Editors' Suggestion

Hydrodynamic thermal transport in silicon at temperatures ranging from 100 to 300 K

Albert Beardo,[1,*,†] Sami Alajlouni,[2,3,*] Lluc Sendra,[1] Javier Bafaluy,[1] Amirkoushyar Ziabari,[4] Yi Xuan,[2,5] Juan Camacho,[1] Ali Shakouri,[2,3] and F. Xavier Alvarez[1]

[1]*Physics Department, Universitat Autònoma de Barcelona, 08193 Bellaterra, Catalonia, Spain*
[2]*Birck Nanotechnology Center, Purdue University, West Lafayette, Indiana 47907, USA*
[3]*School of Electrical and Computer Engineering, Purdue University, West Lafayette, Indiana 47907, USA*
[4]*Oak Ridge National Laboratory, Oak Ridge, Tennessee 37831, USA*
[5]*Department of Surgery, Indiana University School of Medicine, Indiana 46202, USA*

(Received 22 December 2021; accepted 15 March 2022; published 8 April 2022)

The temperature profile around nano- and microscale heat sources on silicon substrate is technologically important for many integrated circuit applications. Here we present full-field thermal imaging of heater lines and rings with different sizes at temperatures ranging from 100 to 300 K. We show significant deviations compared to Fourier's law which are both size and geometry dependent. This can be explained by a hydrodynamic model for heat transport in silicon based on the Guyer and Krumhansl equation using *ab initio* calculated parameters within the kinetic collective model framework. One of these parameters, the nonlocal length, is shown to quantitatively determine the situations where nonFourier behavior occurs. This length scale is some orders of magnitude smaller than the longest phonon mean free paths. Ballistic phonons are shown not to manifest directly in these experiments, thus indicating the failure of the multiscale relaxation time approximation. Furthermore, we discuss the differences between Hamiltonian/microscopic and entropic/mesoscopic strategies to address nanoscale heat transport, and the relations between phonon dynamics and thermodynamics. Finally, the nonequilibrium phonon distribution function is used to determine conditions under which hydrodynamic modeling can be used.

DOI: 10.1103/PhysRevB.105.165303

I. INTRODUCTION

In the last 20 years, many experimental studies of heat transport in silicon and other semiconductors have explored the limit of small and fast excitations. Typically, optical pump-probe with nanoscale transducers [1–4] or electrical excitation with nanoscale heater lines [5,6] are used. Thanks to all these experimental efforts, Fourier's law has been ruled out as a reliable transport equation to describe heat transport in semiconductors at device scales smaller or similar than the phonons mean free path (MFP) [4,5,7,8]. This not only encompasses current nanoscale devices at room temperature but also larger devices at low temperatures. Consequently, the engineering community has been forced to use parametrized numerical tools to predict the heat evolution in nanoscale electronic devices. A simple and predictive transport equation is not only essential for applications, but it is also important to understand the fundamental physics at different length scales. The applications range from heat management in classical electronic devices and phase change materials to quantum computing, spintronics, or energy materials [9–11].

The Boltzmann transport equation (BTE) combined with *ab initio* calculations of phonon dispersion relations and mean free paths has shown to be very powerful to model thermal transport [12–14]. Two different strategies have been pursued. On one hand, within a microscopic framework, one first solves the BTE for each phonon mode and then obtains the observable magnitudes (temperature and heat flux maps) as integral expressions over the different modes [15,16]. The observables are expressed in terms of contributions of the different phonons evolving differently in the sample due to its different mean free paths, making explicit the multiscale nature of the phonon system in the solutions [16]. On the other hand, within a mesoscopic approach, one first integrates the BTE to obtain the equations for a reduced set of moments of the distribution (temperature, heat flux, …) [17–21] that can be directly solved to model experiments. In the latter case, the number of characteristic scales included in the model is reduced because the individual phonon properties participate only through the integral expressions for the mesoscopic equation parameters [6,17,22].

Although it may seem that the two paths are equivalent, an important characteristic of the phonon population gives a very different flavor to each method. According to the relaxation time approximation (RTA) the phonon mean free path spectrum can span several orders in magnitude in semiconductors like silicon, ranging from few nanometers to tens of micrometers [23]. At the nanoscale, this extreme variability introduces large discrepancies in the obtained solutions due to the manifestation of either the multiscale mean free path spectrum or just the few scales associated with the phonon distribution moments within the microscopic and mesoscopic frameworks, respectively. Usually, both approaches can be used to fit the experimental data. In the microscopic framework, strategies

*These authors contributed equally to this work.
†albert.beardo@uab.cat

like the use of phonon suppression functions [1,24] or phenomenological relaxation times to model boundary scattering are used [2,16]. In the mesoscopic models, the free variation of parameters like interfacial thermal boundary resistances or effective thermal conductivities are used [4,8]. This hinders the correct interpretation of the experimental observations as all these fitting strategies essentially hide important physics not included in the models. Therefore, determining whether all the phonons mean free paths or only the reduced set of length scales included in the moment equations are necessary to interpret the thermal evolution of a system, is an important open question. This is crucial to understand thermal transport essentials and envision new applications to engineer and manipulate heat.

Microscopic models are grounded on a Hamiltonian point of view, where the correct determination of collision rates is the most important task to properly describe the phonon system evolution. On the other side, mesoscopic models are based on an entropic point of view, usually represented through a variational principle [25]. Within the latter approach, the determination of a pseudoequilibrium distribution to which the phonon population rapidly decays, due to collisions, is key to model the system thermal response [26]. Provided the collision events are known with full precision, in principle, both approaches are equivalent. However, nonhomogeneous excitations or the influence of the system boundaries, overwhelmingly increase the computational requirements in the Hamiltonian approach, precluding modeling of complex nanoscale samples relevant to technological applications. In such cases, phenomenological simplifications are required, and the equivalence between the Hamiltonian/microscopic and the entropic/mesoscopic approaches is not granted. Connecting both interpretations can open the door to a deeper understanding of the relation between mechanics and thermodynamics.

In recent years, it has been observed that some materials, such as graphene [27–29], seem to show a hydrodynamic-like behavior compatible with the appearance of a single scale, hiding the multiscale nature of the phonon system. Following the mesoscopic path, it can be shown that this regime can be described in stationary experiments by the Guyer and Krumhansl equation (GKE) [30]

$$\vec{q} = -\kappa \nabla T + \ell^2 \nabla^2 \vec{q}, \tag{1}$$

where T is the temperature, $\vec{q}$ is the heat flux, κ is the bulk thermal conductivity, and ℓ is the nonlocal length, which is the only relevant length scale in the regime where Eq. (1) is valid. This behavior has been named phonon hydrodynamics due to the analogy between Eq. (1) and the Navier-Stokes equation used in standard fluid dynamics. Equation (1) is the form of the GKE for stationary situations (steady state), which is the focus of the present work. Additional terms, like a time derivative of the heat flux, may appear in transient situations. We will omit these terms here to simplify the notation. Notice that Eq. (1) can be seen as a generalization of Fourier's law, including an extra viscous term. According to this equation, non-Fourier effects are expected when some of the sample characteristic lengths are comparable to the nonlocal length ℓ. Phonon hydrodynamic heat transport was first successfully applied in the 1960s to understand second sound in materials like NaF [31,32]. It was also used in the last decade to understand the anomalous behavior of thermal transport in two-dimensional (2D) materials like graphene [27,28] or transition metal dichalcogenides [33]. Hydrodynamics has also been applied to 3D materials like graphite [34,35] and black phosphorus [36]. Recently, several experimental results have suggested that semiconductors like silicon or germanium [6,22,37–39] could also be described by the same equation (1) when the experiment's length scale becomes similar to the nonlocal length, but this last interpretation has been controversial.

This controversy has its origin in the works where phonon hydrodynamics was first proposed. In the original work by Guyer and Krumhansl [30], Eq. (1) was derived in the specific situation where the crystal momentum conservation in phonon-phonon collisions is important, that is, when normal phonon-phonon collisions are dominant. This led the community to assume that normal collision dominance was a necessary condition for the GKE to be valid. This is the case for most of the previous materials, but in silicon, normal collisions, despite are present, are not dominant. Therefore, the nanoscale response of silicon has been classified in a different regime called quasi-ballistic, where size effects result from the multiscale nature of phonons [24,40,41]. The usual interpretation is based on suppressing the heat flux contribution of phonons with a mean free path larger than the system size, either by using a suppression function [24], or by using increased thermal boundary resistance (TBR) values in the interface between materials [2,16]. However, this approach seems to be at odds with the wide set of observations in silicon that can be described using Eq. (1) with a single nonlocal scale $\ell \simeq 190$ nm at 300 K [6,22,38,42]. Therefore, elucidating whether the mean free paths larger than the nonlocal length explicitly manifest or not in such experiments is an important open question. Recently, a new derivation of the GKE from the BTE has been obtained without requiring the dominance of normal collisions, which demonstrates the increased applicability of this equation and a microscopic foundation for its use in materials like silicon [20]. This opens the possibility to reinterpret the observed non-Fourier behavior considering this generalized hydrodynamic framework.

II. RESULTS

In this work, we show that the existence of single-scale hydrodynamic transport in silicon is based on solid experimental evidence. Specifically, we demonstrate that it is possible to predict the experimental temperature profile of nanoscale heat sources on silicon substrate with different geometries (circular and linear), various sizes (1–10 microns), and in a wide temperature range (100–300 K), using Eq. (1) along with the energy conservation equation and appropriate boundary conditions (see Appendix C). The two parameters in Eq. (1) are obtained from *ab initio* microscopic calculations in terms of the phonon properties, with no dependence on any length scale from the different devices. This proves that the apparent multiscale behavior in silicon is not manifesting in the present experiments and that phonon hydrodynamics is a fully predictive framework useful for understanding silicon.

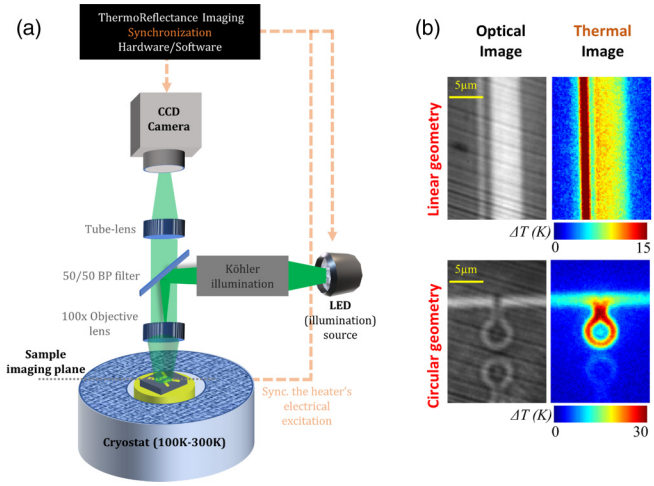

FIG. 1. (a) Thermoreflectance thermal imaging (TRI) setup schematics. The setup utilizes a typical upright microscope with timing hardware/software to synchronize illumination, electrical excitation, and the camera's acquisition. Eventually, a thermal image is produced as shown in (b), and later detailed in Appendix B. The sample under test is placed inside a cryostat to control its temperature. (b) shows sample optical and thermal images for different geometries at 200 K; linear geometry (top) and circular geometry (bottom).

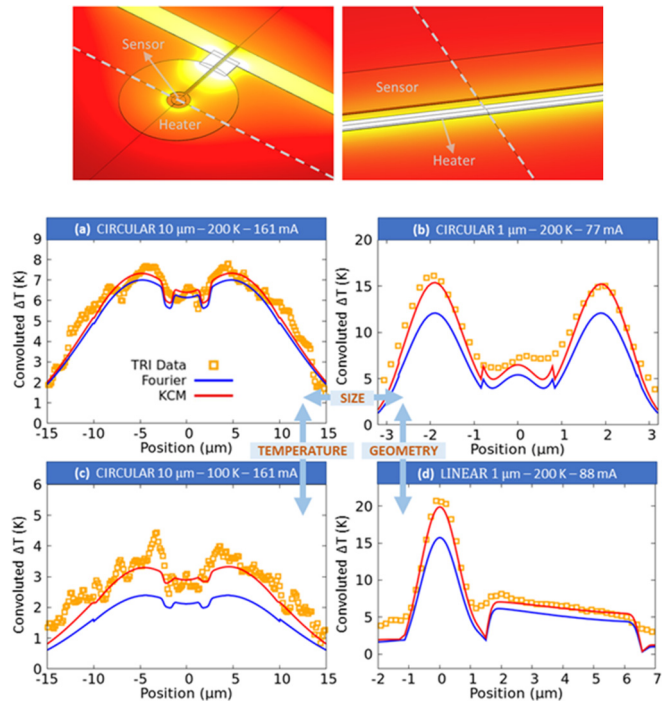

FIG. 2. Stationary temperature profiles on the surface of the sample along the cross sections indicated in the top figures obtained by the thermoreflectance imaging (TRI) setup (orange dots) and the theoretical predictions using bulk Fourier's law (blue line) and Eq. (1) (red line) in the substrate. The theoretical temperature profiles are convoluted with a Gaussian function that captures the imaging setup blurring effects, as explained in the Supplemental Material [53]. The unconvoluted profiles are shown in Figure S2. (a) Large circular heater (width $L = 10\,\mu$m) at 200 K, (b) Small circular heater (width $L = 1\,\mu$m) at 200 K, (c) Large circular heater (width $L = 10\,\mu$m) at 100 K, and (d) Small linear heater (width $L = 1\,\mu$m) at 200 K. The electrical current imposed in the heaters is indicated on top of each profile.

The experimental observations reported in this work comprise thin Au electrical heaters deposited on a Si substrate. The heaters have varying widths from 1–10 μm and two distinct geometries: circular (ring) and linear (straight) heaters. Heat is generated in the heaters via electrical excitation (Joule's heating). Using thermoreflectance imaging (TRI), the steady-state temperature distribution of the heater's top surface, and surrounding Si, is recorded. TRI is an optical technique where surface reflectivity variations can be translated to temperature variations. We measure the Si surface temperature indirectly by deposing a thin layer of Au a few microns away from the heater. This metallization serves as a temperature sensor for the underlying Si layer. Figure 1(b) shows the imaged devices' geometry and sample thermal images. We incorporated a liquid nitrogen cryostat to collect thermal images for varying substrate temperatures (100–300 K). The TRI collects the 2D surface temperature of almost the entire perturbed area. This allows studying the emergence of non-Fourier behavior at cryogenic temperatures locally, not through the system's global or averaged behavior. More details related to the experimental setup are discussed in Appendixes A and B.

In Figs. 2(a)–2(d), the surface temperature profiles along a cross section intersecting the heater and the nearby sensor are shown. To evaluate the viscous effects introduced by the Laplacian term in Eq. (1), the experimental data are compared with finite element solutions using bulk Fourier's law and the GKE for the silicon substrate. The theoretical temperature profiles are convoluted to capture the blurring effects introduced by the cryostat window as explained in the Supplemental Material [53] (see the unconvoluted predictions in Fig. S2). Similar comparisons at room temperature can be found in Ref. [6]. The geometry-independent transport parameters appearing in these equations (κ, ℓ) are calculated from first principles using the microscopic expressions recently obtained in the GKE derivation from the BTE [20]. In the following, we will call the kinetic collective model (KCM) to the combination of Eq. (1) together with the BTE-derived microscopic expressions of its parameters and the appropriate boundary conditions. Remarkably, the KCM uses a TBR value for the metal-semiconductor interface that is fixed (i.e., it is temperature-, geometry-, and size-independent). The required complete system of partial differential transport equations, boundary conditions, and parameter values for different temperatures, is shown in the Appendix C and Table I, respectively.

TABLE I. Temperature-dependent parameter values appearing in Eq. (1) according to the *ab initio* KCM expressions [20] (see Appendix D).

Temperature [K]	300	200	100
Thermal Conductivity κ [W/(m K)]	130	180	400
Non-local length ℓ [nm]	194	389	2149

Figures 2(a) and 2(c) illustrate the first important predictive capability of KCM. At 200 K [Fig. 2(a)], the KCM prediction for the 10-μm circular heater experiment is similar to the Fourier's law one. However, at 100 K in the same geometry [Fig. 2(c)], Fourier and KCM give substantially different results, which highlights the ability of the nonlocal term to capture thermal transport at different temperatures.

The second remarkable observation is that the hydrodynamic model reproduces the experimental thermal profile for different heater sizes. This is highlighted in the transition between Figs. 2(a) and 2(b), where KCM predicts the deviation with respect to Fourier's law when reducing the heater size, while maintaining the same heater circular shape and the same temperature. This effect has been traditionally attributed either to a change in the TBR properties between the heater and the substrate [7,8] or the suppression of the contribution to the conductivity of some phonon modes [1,24]. This has been intensively studied in the last decade from the RTA-BTE approach, and some authors proposed that the interface transmittance should be mode dependent [2,16]. Accordingly, the size of the interface modifies the phonon modes that are injected from the metal to the substrate, thus modifying the effective interfacial resistance [2]. In our experiment, it is important to notice that there is a 20-nm-thick oxide layer between metal and substrate. This oxide layer has an extremely high thermal resistance of $\sim$20 nK m^2/W that hinders the influence of a possible change in the TBR due to size or temperature variations (see Appendix C for details on the characterization of the oxide layer). Nevertheless, the predictions using Eq. (1) for the Si substrate and a fixed TBR value are found to explain the full temperature distribution for different device sizes. Indeed, size effects are accounted for through the Laplacian term in Eq. (1) and, hence, they are decoupled from the resistive effects arising from the TBR. These results are consistent with recent works where the same hydrodynamic modeling together with TBR values very close to the diffuse mismatch model [43] of metal-semiconductor interfaces could explain other experimental configurations in the absence of thick oxide layers [38,42].

A third observation is the impact of complex geometry or the heater shape, which is adequately captured by the hydrodynamic model. In Figs. 2(b) and 2(d), linear and circular structures with the same heater width $L = 1$ μm are compared at the same temperature. In the linear structure, the system has a single length scale (the heater width L) comparable to the nonlocal length. Conversely, in the circular structures, both the heater width L and the radius R are comparable to ℓ. Therefore, to predict the local temperature profile in the circular geometry, and the differences with respect to the linear case, more than a single characteristic system length should be accounted for. This is achieved in the KCM through the Laplacian term in Eq. (1). An extended discussion about the impact of the heater shape on this kind of experiments using the hydrodynamic model at room temperature can be found in Ref. [6].

To summarize the previous results and to highlight the non-Fourier behavior in the present experimental configurations, in Fig. 3, we show the effective thermal conductivity required to fit the heater and the sensor temperature profiles, respectively, if using Fourier's law for the substrate. It displays the fits to the experimental data and to the KCM predicted profiles. Note that the apparent conductivity depends on the region where the temperature profile is fitted – a signature of non-Fourier transport. Remarkably, the KCM captures the measured deviations with respect to the bulk thermal conductivity, which depend on the temperature, the size, and the heater shape. The only exception is the smaller circular geometry at 100 K, where KCM predicts a temperature lower than the ambient one in the sensor. This prediction is not observed in experiments and cannot be fitted using a Fourier's model. More details about the breakdown of KCM in this extreme situation are provided in the Discussion section.

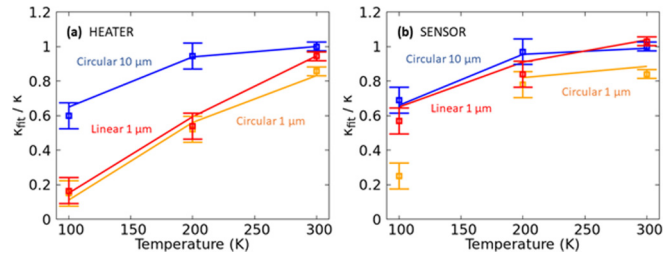

FIG. 3. Normalized effective thermal conductivity of the substrate to fit the temperature profile using Fourier's law (a) in the heater, and (b) in the sensor, for different geometries, sizes, and ambient temperatures. Comparison of the fits to experiments (symbols) and to KCM predictions (lines) is provided. The KCM prediction for the temperature in the sensor of the smaller circular geometry at 100 K is lower than the ambient temperature. Hence, in this case KCM cannot be fitted using an effective Fourier model.

Let us finally emphasize that the accurate predictions of the single-scale hydrodynamic model in such a variety of experiments indicates that the multiscale spectrum of the phonon mean free paths does not manifest in these experiments. This important result and its implications are discussed in the next section.

III. DISCUSSION

We now compare the experimental results and the predictions of the (mesoscopic) hydrodynamic model with those of the (microscopic) RTA-BTE model. To this end, we analyze the substrate's effective thermal diffusivity. This analysis highlights the differences in the thermal response based on the system's size, and the difficulties of describing the present experiments within a microscopic framework. In the traditional RTA-BTE approach, the diffusivity is calculated in terms of the phonon mean free paths Λ_k and the characteristic size of the sample L. This has been described in several works. Here we use the expression obtained in Ref. [44]:

$$\chi = \frac{\sum_k \frac{C_k \Lambda_k^2}{\tau_k (1+\Lambda_k^2 \xi^2)}}{\sum_k \frac{C_k}{1+\Lambda_k^2 \xi^2}}, \tag{2}$$

where $\Lambda_k = v_k \tau_k$ is the mean free path of the phonon mode k, C_k is the mode's specific heat and $\xi \sim 1/L$ is the characteristic reciprocal length scale of the system. Notice that, according to Eq. (2), each phonon mode interacts differently with the scale of the system due to its different phonon mean free path. In the hydrodynamic framework, the effective diffusivity can

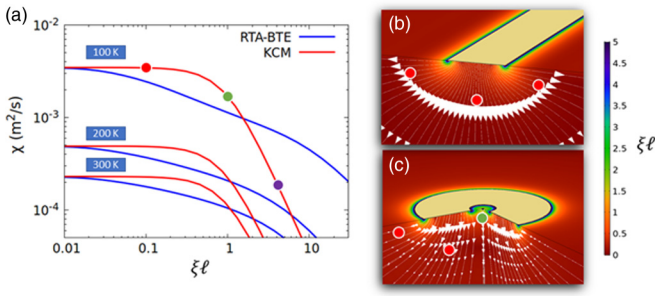

FIG. 4. (a) Effective diffusivity χ vs dimensionless spatial perturbation $\xi\ell$. The blue lines represent the results from RTA-BTE [Eq. (2)], where ξ is the inverse of the heater width. The red lines represent the results from KCM [Eq. (3)], where ξ is the local perturbation obtained from the solution of the Eq. (1). (b), (c) show the magnitude of $\xi\ell$ for (b) the large linear heater, and (c) the large circular heater ($L = 10\,\mu$m) at 100 K, and the white lines represent heat flux streamlines. The dots are selected points intersecting different energy evacuation directions, for which the diffusivity according to Eq. (3) is indicated in plot (a). The blue point in (a) corresponds to a smaller circular geometry displayed in Fig. 5.

be obtained by transforming Eq. (1) to the Fourier space. The resulting effective thermal diffusivity is

$$\chi = \frac{\chi_0}{1 + \ell^2\xi^2}, \tag{3}$$

where χ_0 is the bulk thermal diffusivity, and we can make the natural identification $\xi^2 \simeq |\nabla^2\vec{q}|/|\vec{q}|$.

In Fig. 4(a) we compare the predictions of Eqs. (2) and (3) for silicon at different temperatures. The size dependence predicted by both models differs because of the multiscale nature of RTA (blue line) and the single-scale nature of KCM (red line). Notably, they differ in the length scale where size effects emerge and the effective diffusivity starts to reduce relative to the bulk value by about an order of magnitude within the 100–300 K range. According to the RTA-BTE model, a significant reduction in the effective thermal diffusivity is predicted at characteristic lengths of hundreds of microns at 100 K, which are the values of the largest mean free paths for silicon. Conversely, the hydrodynamic model starts to deviate from the bulk Fourier behavior for significantly smaller L (tens of microns) at the same temperature (since at 100 K, $\ell\sim2\,\mu$m). This latter result is in good agreement with both the data presented in this work and past experiments at room temperature [6,22,38,42], and reveals the failure of the RTA-BTE approach in describing these experiments. Specifically, the length scales corresponding to the largest mean free paths do not manifest. This is evident in Fig. 2(a), where the system size is significantly smaller than the longer phonon MFPs, but no size effects are obtained (i.e., both the KCM prediction and the experimental data are very close to the bulk Fourier prediction). This indicates that the assumption of independent phonon mode evolution and interaction with the system boundaries does not hold for silicon. This conclusion is also supported by the effective conductivity of Si films at room temperature. For example, a 1 μm-thick film displays a conductivity value close to the bulk one, even though there is a significant fraction of thermal phonons with much larger MFPs [22,45]. Numerical solvers of the BTE using the full scattering matrix, including off-diagonal terms, are expected to refine the solutions and describe this kind of experiment. To our knowledge, however, current methods using the full BTE predict the emergence of size effects at length scales even longer than the RTA-BTE model for materials like graphene [46]. This point emphasizes the importance of mesoscopic methods to help disentangle the complexities of the BTE.

Another important difference between models is that, within the RTA-BTE framework, ξ depends on a unique system characteristic length L, whereas, within the hydrodynamic model, ξ can be quantified locally. The simplicity of KCM allows solving Eq. (1) using finite element methods, thus obtaining the thermal response of complex samples without requiring the calculation of any geometry-dependent property. Therefore, the local perturbation $\xi\ell$ map is accessible from the KCM solutions, as shown in Figs. 4(b) and 4(c) for the large circular and linear heaters, respectively, at 100 K. The nonuniform ξ profiles distinguish directions where phonon propagation is more blocked than others (i.e., a different reduction of the local effective thermal diffusivity is obtained depending on the position). Notice that in the straight heater, the value of ξ along different flux streamline directions are similar (red points). In contrast, in the circular geometry, the central region displays larger values of ξ (green point). Therefore, the resulting effective diffusivity depends on the propagation direction in the latter case. This is why these two heaters, with identical linewidths, display different heat dissipation efficiencies according to the hydrodynamic framework. This also explains why, at room temperature, a 1-μm linear heater behaves almost like bulk Fourier while a 1-μm circular one does not have the same behavior [6]. We note that to obtain comparable geometry-dependent modeling within the RTA-BTE framework, not only multiple system length scales should be included in the description, but the effective diffusivity should also depend on the position. Finally, the present analysis could be easily generalized to the presence of other perturbations like, for example, rapidly varying heat sources. In such a situation, other perturbation scales like $\eta \simeq |\partial\vec{q}/\partial t|/|\vec{q}|$ should be used.

The inhomogeneous profile of $\xi^2 \simeq |\nabla^2\vec{q}|/|\vec{q}|$ below the heaters highlights the difficulties of interpreting thermal transport using geometry-dependent effective parameters and offers a new perspective accounting for the vectorial nature of hydrodynamic heat flow. The characteristic lengths over which the phonon population evolves depend on the spatial relaxation of the thermodynamic fluxes ($\vec{q}$ in our case). This imposes restrictions on the phonon population relaxation times, thus precluding microscopic approaches based on the independent evolution of the different phonon modes, like the RTA-BTE framework. Recently, it has been shown that the modification of the relaxation times is a more robust way to interpret the thermal transport in terms of the phonon dynamics [47,48]. The same work also demonstrated that alternative approaches, like the ballistic suppression of phonons [1,24], can give nonunique interpretations under the same conditions.

Moreover, in the last years, it has been shown that the use of alternative descriptions, such as, the relaxon basis diagonalizing the collision operator, can offer a deeper understanding of thermal transport physics in homogeneous nonequilibrium

situations (i.e., under a constant thermal gradient) [14]. Remarkably, it has also been shown that using a modified basis in each position and assuming some phenomenological model for the influence of the boundaries, the applicability of this approach can be extended to simple geometries like thin films [29]. However, under nonhomogeneous perturbations or in the presence of complex boundaries, the drift operator causes transitions between relaxons, thus complicating the solutions in most cases. These difficulties emerge because the microscopic frameworks aim to obtain accurate solutions for the population of heat carriers. Instead, the agreement of KCM with the present experiments indicates that the proper description of the first moments of the distribution function, which are related with mesoscopic quantities like the energy and the heat flux, is enough to understand the general trend of the heat dissipation in our samples, while the exact knowledge of the full carrier distribution is not necessary.

Let us also note that to properly solve the BTE within the RTA approximation, the energy conservation (i.e., the zeroth-order BTE projection) should be imposed to correct the imbalance that the use of an approximate collision operator artificially introduces to the solution [44,49]. Here we suggest that, when the nonequilibrium situation is nonhomogeneous, like for example, near heat sources or system boundaries, the evolution of higher-order moments, like the heat flux, are better modeled in terms of the corresponding higher-order BTE projections than by solving the full BTE. This is achieved through the consistent use of transport equations, transport parameters, and boundary conditions, which are all related through the pseudoequilibrium distribution function (solution of the BTE) as explained in Ref. [20]:

$$f_k = f_k^{\mathrm{eq}} + \vec{\beta}_k \cdot \vec{q} + \overline{\overline{G}}_k : \nabla \vec{q}, \tag{4}$$

where f_k^{eq} is the equilibrium distribution function, $\vec{q}$ is the heat flux and $\vec{\beta}_k$ and $\overline{\overline{G}}_k$ are mode-dependent functions obtained from solving the BTE (see more details in Appendix D).

Additionally, the nonequilibrium distribution function (4) introduced in Ref. [20] can also be used to understand the limits of validity of the hydrodynamic model. It has been observed that when the distance between disconnected boundaries or different heat sources is reduced below the nonlocal length ($\xi\ell > 1$), the effects of the viscous term in silicon are unphysically large [22,38]. In the present experiments, we have one case beyond the KCM applicability in silicon (determined in Ref. [22]), which is the small circular line at 100 K ($\mathrm{L} = 1\ \mu\mathrm{m} < \ell,\ \mathrm{R} = 2\ \mu\mathrm{m} \sim \ell$). As shown in Fig. 5(a), the *ab initio* KCM model fails to describe the temperature distribution in this case. Specifically, the model predicts negative values of ΔT (i.e., cooling) at the center of the structure that are not observed in experiments. Remarkably, similar cooling effects have been predicted and observed in transient experiments in other materials where normal phonon-phonon collisions dominate [50], which might allow distinguishing hydrodynamic effects in kinetic (like silicon) and collective (like graphene) materials [51]. Nevertheless, it is worth noting that the hydrodynamic model with the use of fitted effective parameters $\kappa_{\mathrm{ef}} = 100\,\mathrm{W/(m\,K)}$ and $\ell_{\mathrm{ef}} = 500\,\mathrm{nm}$ [magenta line in Fig. 5(a)] fits the full experimental profile, whereas effective Fourier's law cannot.

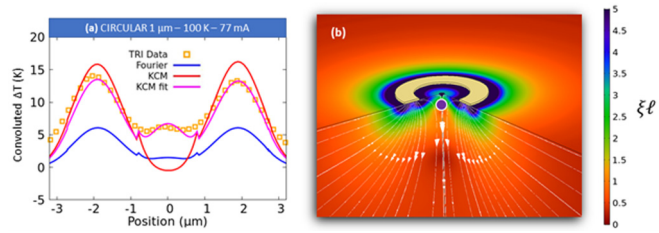

FIG. 5. (a) Stationary temperature profile on the surface of the sample at 100 K obtained by the TRI setup (orange squares) and the convoluted predictions using Fourier's law (blue line), Eq. (1) (red line), and Eq. (1) with effective fitted parameters (magenta line). (b) Magnitude of $\boldsymbol{\xi}\ell$ for the small circular heater ($L = 1\ \mu$m, $R = 2\ \mu$m) at 100 K. The white lines represent the heat flux streamlines. The blue dot is a selected point for which the diffusivity according to Eq. (3) is represented in Fig. 4(a).

To understand the breakdown of KCM in this situation, we calculate the distribution function f_k corresponding to our hydrodynamic solution (see details in Appendix D). Expression (4) can be locally evaluated from the thermodynamic magnitudes obtained within the finite element solution of the KCM. In Fig. 6, we show f_k for two different situations: one where the hydrodynamic model is predictive [green dot in Fig. 4(c), where $\xi\ell = 1$], and other corresponding to the breakdown of the model [blue dot in Fig. 5(b), where $\xi\ell = 5$]. In the situation where KCM is predictive, Eq. (4) gives positive values

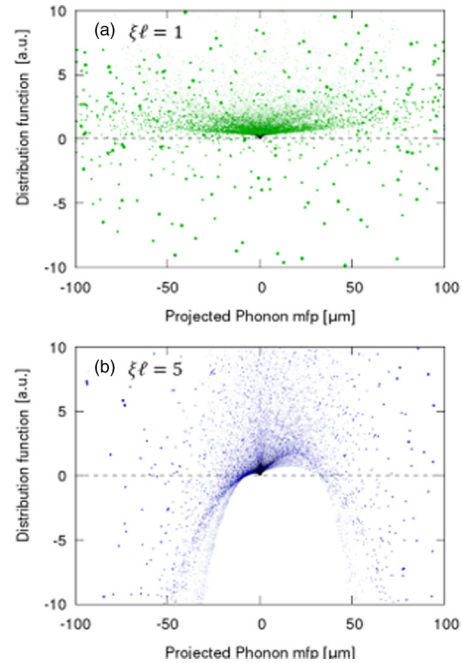

FIG. 6. Phonon distribution function [Eq. (4)] at 100 K in the direction of the temperature gradient, $\Lambda_k \cos\theta$, where θ is the angle between the phonon velocity and the temperature gradient. (a) Local distribution at the green point below the large circular heater displayed in Fig. 4(c) ($\xi\ell = 1$), and (b) at the blue point below the small circular heater displayed in Fig. 5(b) ($\xi\ell = 5$). An unphysical distribution function (negative populations) is obtained for $\xi\ell = 5$, which is beyond the applicability of KCM.

for almost all the phonon modes [Fig. 6(a)]. Only a reduced number of points that are associated with numerical error have negative (unphysical) populations, but these phonons represent less than 5% of the thermal conductivity. On the contrary, in the situation where KCM does not work, negative (unphysical) phonon populations represent a significant subset of the distribution with a non-negligible contribution to the thermal conductivity [Fig. 6(b)]. In this situation, the description of the thermal behavior in terms of a single length scale ℓ is inadequate. In such case, higher-order distribution moments may be participating in the system's thermal evolution and a more complex pseudo-equilibrium distribution function, and transport equation, are required to model its response.

IV. CONCLUSION

In summary, we have shown the application of the hydrodynamic Eq. (1) to describe the thermal behavior of microscale heat sources of different sizes and geometries on a silicon substrate in a wide ambient temperature range. The Guyer-Krumhansl equation is shown to capture most of the discrepancies between bulk Fourier's law and experiments using a single length scale ℓ. Conversely, the present experiments cannot be solely explained using the multiscale nature of the phonons mean-free-paths, in silicon. Moreover, the hydrodynamic equation allows for a better understanding of the transport behavior in complex geometries. Two parameters are necessary to characterize the thermal behavior of the devices under study, namely the thermal conductivity and the nonlocal length, which can be easily calculated from first-principles calculations based on the BTE [20] (shown in Table I). On the other hand, the temperature profile around small circular heater (width $L = 1\,\mu$m and radius $R = 2\,\mu$m) at 100 K, deviates from the hydrodynamic model predictions. This is consistent with previous experiments on silicon, which showed that the hydrodynamic model with *ab initio* parameters fails to describe adjacent heat sources closer than the nonlocal length [38]. Here, we have shown that this failure has its microscopic counterpart, namely, the nonequilibrium phonon distribution displays negative values and thus becomes unphysical in such situations. This indicates the need to include the influence of higher phonon distribution moments to extend the KCM applicability to smaller length scales.

ACKNOWLEDGMENT

A.B, L.S., J.B., J.C., and F.X.A., acknowledge financial support by the Spanish Ministerio de Ciencia, Innovación y Universidades under Grant No. RTI2018-097876−B-C22 (MCIU/AEI/FEDER, UE).

APPENDIX A: DEVICE FABRICATION

A 20-nm Al_2O_3 film was deposited at 200 °C on a p-type Si wafer (resistivity of 10–20 ohm cm) by atomic layer deposition. The film was annealed at 450 °C for 30 s. Finally, a 100-nm Au layer was deposited on top of ∼5 nm Ti layer using electron-beam lithography, metallization, and lift-off processes. The thin Ti layer improves the Au surface adhesion. The Au was patterned into heaters of varying widths (1–10 μm) with two distinct geometries; circular and linear (straight) heaters [as shown in Fig. 1(b)]. Heat is generated in Au via electrical excitation (Joule heating), then a thermal image is acquired using the thermoreflectance (TR) technique.

APPENDIX B: THERMOREFLECTANCE IMAGING (TRI)

The experimental imaging setup is shown in Fig. 1(a). Thermoreflectance thermal imaging (TRI) is a high-resolution, noncontact optical imaging technique where the sample's top surface reflectivity varies as a function of temperature [52]. The device under test (DUT) is electrically excited with a pulse-train switching between on and off states. During the on state, the DUT self-heats due to Joule heating, and the surface reflection coefficient changes as a function of temperature. During the off state, the DUT relaxes back to the ambient temperature. A CCD camera quantifies the thermally induced optical reflectivity variations between the on and off states ($\Delta R/R_{\text{off}}$), which finally produces a full-field 2D thermal image (spatial temperature distribution) of the top surface. To a first-order approximation, ($\Delta R/R$) correlates linearly with the surface's temperature change (ΔT). The linear correlation coefficient (C_{TH}) is a function of the illumination wavelength, the sample's material, and surface characteristics. We use a green ($\lambda = 530\,$nm) LED to illuminate our tested devices. The value of the (C_{TH}) can be calibrated in multiple ways. Our calibration methods are detailed in [6]. Calibrated (C_{TH}) values for Au and Si were measured to be $-2.2 \times 10^{-4} \pm 5\%$ and $1 \times 10^{-4} \pm 5\%$ respectively.

Using TRI, the top surface's steady-state temperature distribution (thermal image) is captured after 500μs of electrical excitation (Joule heating). The $\lambda = 530\,$nm illumination in conjunction with a 100x air objective lens (NA = 0.75) provides a typical spatial resolution of ∼430 nm. We used a Janis ST-500 liquid nitrogen cryostat to vary the DUT's temperature from 300 K down to 100 K. The cryostat has a glass window. This window situated between the standard objective and the sample adds extra blurring to the thermal image. By comparing images with and without the cryostat's window at room temperature while keeping all other experimental conditions the same, we extracted the window's blurring function. This blurring function is assumed to be temperature-independent, and it is used to convolute the theoretical predictions for comparison with experimental data at low temperatures (see details in the Supplemental Material [53]).

TRI requires some time averaging (over multiple cycles) to improve the thermal resolution of the image. The thermal images acquired for the Au structures were averaged for 1–5 minutes yielding a typical resolution of 0.1 K.

APPENDIX C: KINETIC COLLECTIVE MODEL (KCM)

We show here the complete system of partial differential equations and boundary conditions required for predicting the heat flux $\vec{q}$, the temperature T, and the electrical current density $\vec{J}$ in our samples using finite element methods [22].

1. Transport equations

Heat conduction in the 100-nm-thick metal domains (composed of gold) is described using conservation of energy, including Joule's heating along with Fourier's law,

$$\nabla \cdot \vec{q}_\Gamma = \rho(\vec{J} \cdot \vec{J}), \tag{A1}$$

$$\vec{q}_\Gamma + \kappa_{Au} \nabla T_\Gamma = 0, \tag{A2}$$

where $\kappa_{Au} = 310\,\mathrm{W/m\,K}$ is the gold bulk thermal conductivity, and

$$\rho = \rho_0(1 + \alpha(T_\Gamma - T_0)) \tag{A3}$$

is the electrical resistivity with $\rho_0 = 29\Omega\,\mathrm{nm}$, $\alpha = 0.0028\,\mathrm{K}^{-1}$, and $T_0 = 295\,\mathrm{K}$ the reference temperature. The temperature T and the heat flux $\vec{q}$ in the metal domains are denoted by subindex Γ. The current density is determined by imposing the following conservation equation

$$\nabla \cdot \vec{J} = 0. \tag{A4}$$

Finally, thermal transport in the silicon substrate is described using conservation of energy and the stationary hydrodynamic heat transport equation

$$\nabla \cdot \vec{q} = 0, \tag{A5}$$

$$\vec{q} + \kappa \nabla T = \ell^2 \nabla^2 \vec{q}, \tag{A6}$$

where κ is the silicon bulk thermal conductivity, and ℓ is the nonlocal length. The temperature-dependent values for these parameters can be found in Table I. Its microscopic expressions in terms of the phonon lifetimes and velocities can be found in Ref. [20]. Note that we assume high impurity concentration in the silicon substrate of the samples under consideration as characterized in previous work [6]. This translates to a slight reduction of the bulk thermal conductivity relative to natural silicon, whereas the nonlocal length values are not significantly modified.

2. Boundary conditions

The metal domains are electrically insulated,

$$\vec{J} \cdot \vec{n} = 0, \tag{A7}$$

except in the heater terminals, in which a current intensity i is imposed,

$$\int \vec{J} \cdot \vec{n} dS = i, \tag{A8}$$

where $\vec{n}$ is the boundary-normal vector. In the thermometer sensors, no current intensity is imposed $\vec{J} = 0$.

In both the heater and the sensor free surfaces, thermal insulation is imposed,

$$\vec{q}_\Gamma \cdot \vec{n} = 0. \tag{A9}$$

Moreover, there is a 20-nm-thick oxide layer between the metal and the semiconductor. This layer obeys Fourier's law with conductivity $\kappa_{\mathrm{ox}} = 1\,\mathrm{W/mK}$. Characterization of the thermal conductivity of the oxide layer for the same samples was performed in Ref. [6]. In the metal-oxide interface, continuity of the heat flux and the temperature is imposed. Hence, subindex Γ is also used to identify the thermodynamic magnitudes in the oxide layer. In the oxide-silicon interface, we impose three conditions to connect Fourier and hydrodynamic transport [42]. The first is continuity of the normal component of the heat flux,

$$\vec{q}_\Gamma \cdot \vec{n} = \vec{q} \cdot \vec{n}. \tag{A10}$$

The second is a temperature jump boundary condition that accounts for the nonequilibrium effects introduced by the interface

$$T - T_\Gamma = \gamma^{-1}(\beta \nabla \cdot \vec{q} - \bar{\bar{\chi}} : \nabla \vec{q}), \tag{A11}$$

where γ, β, $\bar{\bar{\chi}}$ are *ab initio* calculated coefficients. Derivation of this boundary condition, the temperature-dependent parameter values, and the microscopic expression for the appearing coefficients can be found elsewhere [42]. In the present experiment, the main contribution to the temperature jump between the metal and the semiconductor is due to the presence of the oxide layer, which plays the role of the usual Kapitza interface resistance. Further reduction of the interface size L is required to observe a significant contribution of nonequilibrium effects predicted by Eq. (A11) even at low temperatures.

Finally, the third condition is a slip boundary condition for the tangential component of the substrate heat flux $\vec{q}_t$ [22]:

$$\vec{q}_t = C\ell \nabla \vec{q}_t \cdot \vec{n}, \tag{A12}$$

where $\vec{n}$ points towards the substrate. The slip coefficient C depends on the fraction of specular phonon reflections in the boundary, as discussed in Ref. [22]. Here we assume diffusive boundary reflections so that $C = 1$.

In the substrate free-surfaces, insulation (A9) for the normal component of $\vec{q}$ and the slip boundary condition (A12) for its tangential component are imposed. We note that the presence of heat flux boundary layers [22] far away from the heat sources in the substrate top surface has a negligible effect in the present experimental conditions. Consistently, the value of C does not significantly modify the temperature profile predictions. Finally, the temperature of the substrate base is fixed to the cryostat temperature.

APPENDIX D: NONEQUILIBRIUM PHONON DISTRIBUTION FUNCTION

In Ref. [20], the distribution function (4) is used to derive the hydrodynamic transport Eq. (A6) from the momentum projection of the BTE, in terms of the unknown functions $\vec{\beta}_k$ and $\overline{\overline{G}}_k$. These functions are obtained by solving the BTE, thus providing microscopic expressions for the transport parameters κ and ℓ. The crucial idea is to assume an expansion of the phonon distribution in terms of the heat flux and its gradients, which are assumed to be independent thermodynamic variables.

Simple expressions for the functions $\vec{\beta}_k$ and $\overline{\overline{G}}_k$ in terms of phonon velocities and relaxation times can be obtained by assuming RTA as shown in Ref. [20]. For silicon, this approximation provides values very close to the exact solution, which can be obtained by iterative methods. In this work, the RTA expressions for $\vec{\beta}_k$ and $\overline{\overline{G}}_k$ are used to calculate from first principles the transport parameters at different

temperatures (Table I), and the nonequilibrium distribution function (4). In Fig. 6, the latter is evaluated in different points using the local heat flux and local heat flux gradient as obtained from the FEM solutions of the hydrodynamic heat transport model (Appendix C). Even though RTA is used to simplify the microscopic calculations, the hydrodynamic framework is not equivalent to directly solve the BTE under the RTA, which provides a significantly different phenomenology as discussed in the present work. It is also worth to note that the connection between the mesoscopic transport equation and the nonequilibrium distribution function allows to consistently obtain the required boundary conditions by imposing microscopic magnitude balances in the boundaries [26,42].

[1] Y. Hu, L. Zeng, A. J. Minnich, M. S. Dresselhaus, and G. Chen, Spectral mapping of thermal conductivity through nanoscale ballistic transport, Nat. Nanotechnol. **10**, 701 (2015).

[2] C. Hua, X. Chen, N. K. Ravichandran, and A. J. Minnich, Experimental metrology to obtain thermal phonon transmission coefficients at solid interfaces, Phys. Rev. B **95**, 205423 (2017).

[3] K. T. Regner, D. P. Sellan, Z. Su, C. H. Amon, A. J. H. McGaughey, and J. A. Malen, Broadband phonon mean free path contributions to thermal conductivity measured using frequency domain thermoreflectance, Nat. Commun. **4**, 1640 (2013).

[4] R. B. Wilson and D. G. Cahill, Anisotropic failure of fourier theory in time-domain thermoreflectance experiments, Nat. Commun. **5**, 5075 (2014).

[5] A. Ziabari, P. Torres, B. Vermeersch, Y. Xuan, X. Cartoixa, A. Torello, J.-H. Bahk, Y. R. Koh, M. Parsa, P. D. Ye, F. X. Alvarez, and A. Shakouri, Full-field thermal imaging of quasiballistic crosstalk reduction in nanoscale devices, Nat. Commun. **9**, 255 (2018).

[6] S. Alajlouni, A. Beardo, L. Sendra, A. Ziabari, J. Bafaluy, J. Camacho, Y. Xuan, F. X. Alvarez, and A. Shakouri, Geometrical quasi-ballistic effects on thermal transport in nanostructured devices, Nano Res. **14**, 945 (2021).

[7] M. E. Siemens, Q. Li, R. Yang, K. A. K. K. A. Nelson, E. H. Anderson, M. M. Murnane, and H. C. Kapteyn, Quasi-ballistic thermal transport from nanoscale interfaces observed using ultrafast coherent soft x-ray beams, Nat. Mater. **9**, 26 (2010).

[8] K. M. Hoogeboom-Pot, J. N. Hernandez-Charpak, X. Gu, T. D. Frazer, E. H. Anderson, W. Chao, R. W. Falcone, R. Yang, M. M. Murnane, H. C. Kapteyn, and D. Nardi, A new regime of nanoscale thermal transport: Collective diffusion increases dissipation efficiency, Proc. Natl. Acad. Sci. **112**, 201503449 (2015).

[9] H. Adachi and S. Maekawa, Thermal effects in spintronics: Physics and applications, in *Handbook of Spintronics* (Springer, Dordrecht, 2016), pp. 1553–1576.

[10] M. Partanen, K. Y. Tan, J. Govenius, R. E. Lake, M. K. Mäkelä, T. Tanttu, and M. Möttönen, Quantum-limited heat conduction over macroscopic distances, Nat. Phys. **12**, 460 (2016).

[11] G. Zhang and W. Duan, Advanced materials for heat energy transfer, conversion, storage, and utilization, Adv. Funct. Mater. **30**, 1907882 (2020).

[12] K. Esfarjani and H. Stokes, Method to extract anharmonic force constants from first principles calculations, Phys. Rev. B **77**, 144112 (2008).

[13] A. Ward and D. A. Broido, Intrinsic phonon relaxation times from first-principles studies of the thermal conductivities of Si and Ge, Phys. Rev. B **81**, 085205 (2010).

[14] A. Cepellotti and N. Marzari, Thermal Transport in Crystals as a Kinetic Theory of Relaxons, Phys. Rev. X **6**, 041013 (2016).

[15] L. Lindsay, D. A. Broido, and T. L. Reinecke, *Ab initio* thermal transport in compound semiconductors, Phys. Rev. B **87**, 165201 (2013).

[16] C. Hua, L. Lindsay, X. Chen, and A. J. Minnich, Generalized Fourier's law for nondiffusive thermal transport: Theory and experiment, Phys. Rev. B **100**, 085203 (2019).

[17] M. Simoncelli, N. Marzari, and A. Cepellotti, Generalization of Fourier's Law Into Viscous Heat Equations, Phys. Rev. X **10**, 011019 (2020).

[18] Y. Guo and M. Wang, Phonon hydrodynamics for nanoscale heat transport at ordinary temperatures, Phys. Rev. B **97**, 035421 (2018).

[19] Y. Guo, D. Jou, and M. Wang, Nonequilibrium thermodynamics of phonon hydrodynamic model for nanoscale heat transport, Phys. Rev. B **98**, 104304 (2018).

[20] L. Sendra, A. Beardo, P. Torres, J. Bafaluy, F. X. Alvarez, and J. Camacho, Derivation of a hydrodynamic heat equation from the phonon boltzmann equation for general semiconductors, Phys. Rev. B **103**, L140301 (2021).

[21] Y. Dong, B.-Y. Cao, and Z.-Y. Guo, Generalized heat conduction laws based on thermomass theory and phonon hydrodynamics, J. Appl. Phys. **110**, 063504 (2011).

[22] A. Beardo, M. Calvo-Schwarzwälder, J. Camacho, T. G. Myers, P. Torres, L. Sendra, F. X. Alvarez, and J. Bafaluy, Hydrodynamic Heat Transport in Compact and Holey Silicon Thin Films, Phys. Rev. Appl. **11**, 034003 (2019).

[23] K. Esfarjani, G. Chen, and H. T. Stokes, Heat transport in silicon from first-principles calculations, Phys. Rev. B **84**, 085204 (2011).

[24] L. Zeng, K. C. Collins, Y. Hu, M. N. Luckyanova, A. A. Maznev, S. Huberman, V. Chiloyan, J. Zhou, X. Huang, K. A. Nelson, and G. Chen, Measuring phonon mean free path distributions by probing quasiballistic phonon transport in grating nanostructures, Sci. Rep. **5**, 17131 (2015).

[25] J. M. Ziman, *Electrons and Phonons: The Theory of Transport Phenomena in Solids* (Oxford University Press, Oxford, 2001).

[26] H. Struchtrup, *Macroscopic Transport Equations for Rarefied Gas Flows* (Springer-Verlag, Berlin, 2005).

[27] S. Lee, D. A. Broido, K. Esfarjani, and G. Chen, Hydrodynamic phonon transport in suspended graphene, Nat. Commun. **6**, 6290 (2015).

[28] A. Cepellotti, G. Fugallo, L. Paulatto, M. Lazzeri, F. Mauri, and N. Marzari, Phonon hydrodynamics in two-dimensional materials, Nat. Commun. **6**, 6400 (2015).

[29] A. Cepellotti and N. Marzari, Boltzmann transport in nanostructures as a friction effect, Nano Lett. **17**, 4675 (2017).

[30] R. A. Guyer and J. A. Krumhansl, Solution of the linearized phonon Boltzmann equation, Phys. Rev. **148**, 766 (1966).
[31] H. E. Jackson, C. T. Walker, and T. F. McNelly, Second Sound in NaF, Phys. Rev. Lett. **25**, 26 (1970).
[32] R. Kovács and P. Ván, Second sound and ballistic heat conduction: NaF experiments revisited, Int. J. Heat Mass Transf. **117**, 682 (2018).
[33] P. Torres, F. X. Alvarez, X. Cartoixà, and R. Rurali, Thermal conductivity and phonon hydrodynamics in transition metal dichalcogenides from first-principles, 2D Mater. **6**, 035002 (2019).
[34] S. Huberman, R. A. Duncan, K. Chen, B. Song, V. Chiloyan, Z. Ding, A. A. Maznev, G. Chen, and K. A. Nelson, Observation of second sound in graphite at temperatures above 100 K, Science **364**, 375 (2019).
[35] Z. Ding, J. Zhou, B. Song, V. Chiloyan, M. Li, T.-H. Liu, and G. Chen, Phonon hydrodynamic heat conduction and knudsen minimum in graphite, Nano Lett. **18**, 638 (2018).
[36] K. Izawa, A. Miyake, Y. Machida, M. Tokunaga, K. Akiba, A. Subedi, K. Behnia, and Y. Akahama, Observation of Poiseuille flow of phonons in black phosphorus, Sci. Adv. **4**, eaat3374 (2018).
[37] A. Beardo, M. López-Suárez, L. A. Pérez, L. Sendra, M. I. Alonso, C. Melis, J. Bafaluy, J. Camacho, L. Colombo, R. Rurali, F. X. Alvarez, and J. S. Reparaz, Observation of second sound in a rapidly varying temperature field in Ge, Sci. Adv. **7**, eabg4677 (2021).
[38] A. Beardo, J. L. Knobloch, L. Sendra, J. Bafaluy, T. D. Frazer, W. Chao, J. N. Hernandez-Charpak, H. C. Kapteyn, B. Abad, M. M. Murnane, F. X. Alvarez, and J. Camacho, A general and predictive understanding of thermal transport from 1D- and 2D-Confined nanostructures: Theory and experiment, ACS Nano **15**, 13019 (2021).
[39] R. Kovács, Analytic solution of Guyer-Krumhansl equation for laser flash experiments, Int. J. Heat Mass Transf. **127**, 631 (2018).
[40] J. A. Johnson, A. A. Maznev, J. Cuffe, J. K. Eliason, A. J. Minnich, T. Kehoe, C. M. S. Torres, G. Chen, and K. A. Nelson, Direct Measurement of Room-Temperature Nondiffusive Thermal Transport Over Micron Distances in a Silicon Membrane, Phys. Rev. Lett. **110**, 025901 (2013).
[41] A. A. Maznev and J. A. Johnson, Onset of nondiffusive phonon transport in transient thermal grating decay, Phys. Rev. B **84**, 195206 (2011).
[42] A. Beardo, M. G. Hennessy, L. Sendra, J. Camacho, T. G. Myers, J. Bafaluy, and F. X. Alvarez, Phonon hydrodynamics in frequency-domain thermoreflectance experiments, Phys. Rev. B **101**, 075303 (2020).
[43] E. Swartz and R. Pohl, Thermal boundary resistance, Rev. Mod. Phys. **61**, 605 (1989).
[44] B. Vermeersch, J. Carrete, N. Mingo, and A. Shakouri, Superdiffusive heat conduction in semiconductor alloys. I. Theoretical Foundations, Phys. Rev. B **91**, 085202 (2015).
[45] E. A. Scott, C. Perez, C. Saltonstall, D. P. Adams, V. Carter Hodges, M. Asheghi, K. E. Goodson, P. E. Hopkins, D. Leonhardt, and E. Ziade, Simultaneous thickness and thermal conductivity measurements of thinned silicon from 100 nm to 17 μm, Appl. Phys. Lett. **118**, 202108 (2021).
[46] V. Chiloyan, S. Huberman, Z. Ding, J. Mendoza, A. A. Maznev, K. A. Nelson, and G. Chen, Green's functions of the Boltzmann transport equation with the full scattering matrix for phonon nanoscale transport beyond the relaxation-time approximation, Phys. Rev. B **104**, 245424 (2021).
[47] M. Forghani and N. G. Hadjiconstantinou, Comparison on two ways of phonon spectral property reconstruction from thermal spectroscopy experiment, Int. J. Heat Mass Transf. **175**, 121119 (2021).
[48] M. Forghani and N. G. Hadjiconstantinou, Phonon relaxation time reconstruction from transient thermal grating experiments and comparison with density functional theory predictions, Appl. Phys. Lett. **114**, 023106 (2019).
[49] B. Vermeersch, A. M. S. Mohammed, G. Pernot, Y. R. Koh, and A. Shakouri, Superdiffusive heat conduction in semiconductor alloys. II. truncated lévy formalism for experimental analysis, Phys. Rev. B **91**, 085203 (2015).
[50] J. Jeong, X. Li, S. Lee, L. Shi, and Y. Wang, Transient Hydrodynamic Lattice Cooling by Picosecond Laser Irradiation of Graphite, Phys. Rev. Lett. **127**, 085901 (2021).
[51] C. Zhang and Z. Guo, A transient heat conduction phenomenon to distinguish the hydrodynamic and (quasi) ballistic phonon transport, Int. J. Heat Mass Transf. **181**, 121847 (2021).
[52] M. Farzaneh, K. Maize, D. Lüerßen, J. A. Summers, P. M. Mayer, P. E. Raad, K. P. Pipe, A. Shakouri, R. J. Ram, and J. A. Hudgings, CCD-Based Thermoreflectance Microscopy: Principles and Applications, J. Phys. D **42**, 143001 (2009).
[53] See Supplemental Material at http://link.aps.org/supplemental/10.1103/PhysRevB.105.165303 for detailed description about the characterization of the blurring effects introduced by the cryostat window with finite thickness.